Communications Biology

https://doi.org/10.1038/s42003-026-09648-1

Article in Press

Selective binding of divalent cations reshapes nucleosome mechanics and unlocks histone tail dynamics

Received: 15 September 2025

Accepted: 26 January 2026

Cite this article as: Hu, G., Zhang, H., Xu, W. *et al.* Selective binding of divalent cations reshapes nucleosome mechanics and unlocks histone tail dynamics. *Commun Biol* (2026). https://doi.org/10.1038/s42003-026-09648-1

Guanhua Hu, Houfang Zhang, Wang Xu, Gege Liu & Yunhui Peng

Selective Binding of Divalent Cations Reshapes Nucleosome Mechanics and Unlocks Histone Tail Dynamics

Guanhua Hu, Houfang Zhang, Wang Xu, Gege Liu and Yunhui Peng*

Institute of Biophysics and Department of Physics, Central China Normal University, Wuhan, 430079, China

*Correspondence: Yunhui Peng: yunhuipeng@ccnu.edu.cn

Abstract

Divalent cations such as Mg^{2+} and Ca^{2+} are key modulators of chromatin architecture, yet their atomistic influence on nucleosome structure and histone tail dynamics remains elusive. Here, we present 81 microseconds of all-atom molecular dynamics (MD) simulations to dissect how these ions shape nucleosome dynamics and plasticity. We quantitively mapped the selective binding patterns of Mg^{2+} and Ca^{2+} in nucleosomes with and without histone tails, revealing distinct ion–nucleosome interactions. Notably, divalent ion binding reduces inter-gyre electrostatic repulsion, facilitates DNA gyre compaction, and increases nucleosome stiffness, as quantified by estimates of the Young's modulus and correlated motions within specific DNA regions. Importantly, ion binding weakens histone tail–DNA interactions and enhances tail mobility—particularly that of H3—potentially facilitating access by chromatin regulators and tail-mediated chromatin compaction. These findings reveal a dual role of divalent ions in modulating nucleosome plasticity while reinforcing histone tail dynamics, providing a mechanistic framework for understanding how ionic fluctuations influence gene accessibility and chromatin state.

Key words

Nucleosome dynamics; Divalent ions; Histone tail flexibility; DNA compaction; Chromatin remodeling; MD simulations

Introduction

Ions are indispensable regulators of chromatin architecture and genome function, shaping the physicochemical environment of the nucleus[1-3]. Among them, divalent cations such as Mg^{2+} and Ca^{2+} are critical for chromatin integrity and compaction. By neutralizing electrostatic repulsion between negatively charged DNA helices, these ions promote higher-order folding and modulate the biophysical state of the genome[4-7]. Fluctuations in their nuclear concentrations influence chromosome condensation, nucleosome accessibility, and transcription during processes such as differentiation, cell cycle progression, and stress response[2,3,8-10]. Localized changes in Ca^{2+} or Mg^{2+} levels—frequently accompanying signal transduction or disease—highlight their potential as dynamic regulators of genome organization[11-13].

At the heart of chromatin lies the nucleosome, a ~147 bp DNA segment wrapped around a histone octamer, whose stability and conformation are maintained by a finely balanced electrostatic network[14,15]. Acting as a polyelectrolyte, the nucleosome generates a strong negative electrostatic field that governs local compaction and the recruitment of chromatin remodelers, transcription factors, and histone modifiers[16-18]. While monovalent ions broadly influence chromatin behavior, divalent cations interact with DNA grooves and histone–DNA interfaces with higher affinity and specificity, exerting more targeted structural effects[19-21]. Recent evidence suggests that these ions can partially substitute for histone tails in stabilizing nucleosomes or act synergistically with linker histones to fine-tune chromatin accessibility[7,21].

Beyond structural stabilization, nuclear divalent cation levels appear to be actively tuned by metabolic cues. For example, transient elevations in nuclear ATP observed in hormone-stimulated cells can promote chromatin opening by chelating free Mg^{2+}, whereas subsequent ATP hydrolysis releases Mg^{2+} to drive chromatin re-condensation[22-24]. This ATP–Mg^{2+} cycling may define a precise temporal window of transcriptional accessibility through dynamic phase separation, thus coupling cellular energy status to chromatin structural transitions.

Despite these insights, the atomistic mechanisms by which Mg^{2+} and Ca^{2+} modulate nucleosome architecture, DNA gyre geometry, and histone tail dynamics remain poorly resolved. Although numerous atomistic simulations have examined the conformational dynamics of nucleosomal histone tails and their interactions with DNA, most have been performed under physiological monovalent salt conditions without accounting for the effects of divalent ions[25-28]. Prior coarse-grained and implicit-solvent simulations have linked ionic conditions to global chromatin folding and phase behavior[29-31], but have lacked the spatial and temporal resolution needed to map specific ion-binding sites and their consequences for nucleosome mechanics. This gap is important because histone tail flexibility and DNA exposure directly impact the

recruitment of chromatin regulators and the establishment of epigenetic states. Moreover, nucleosome mechanical plasticity has been associated with liquid–liquid phase separation, suggesting that nanoscale changes in nucleosome stiffness may have far-reaching effects on genome function[32-35].

Here, we bridge this gap using 81 μs of all-atom MD simulations to dissect how Mg^{2+} and Ca^{2+} regulate nucleosome conformation, DNA gyre spacing, and histone tail behavior. We mapped ion-binding landscapes in nucleosomes with and without histone tails, and quantified their effects on DNA compaction, nucleosome height, and mechanical stiffness. We find that divalent cations preferentially accumulate in DNA grooves, along the phosphate backbone, and in inter-gyre regions, where they neutralize electrostatic repulsion, promote tighter gyre wrapping, and increase nucleosome stiffness and correlated motions within specific DNA regions. Concomitantly, ion binding disrupts histone tail–DNA contacts and enhances tail mobility—particularly in H3—potentially facilitating the recruitment of chromatin regulators and tail-mediated chromatin compaction.

Our findings reveal a dual mechanism by which divalent cations modulating nucleosome plasticity while reinforcing histone tail dynamics. This atomistic framework provides new mechanistic insight into how ionic microenvironments shape nucleosome mechanics, linking physical chemistry to chromatin organization, epigenetic regulation, and nuclear responses to metabolic or signaling cues.

Results

Higher local ion density of divalent cations highlights their preferential association with the nucleosome

We constructed nucleosome systems under multiple ionic conditions in Simulation Sets 1 and 2 (Figure 1a; Supplementary Tables 1–3). To probe the spatial distribution of ions around the nucleosome, we computed radial distribution functions (RDFs) across different simulation setups (Figure 1b). Divalent cations accumulated at markedly higher local densities near the nucleosome compared to monovalent Na^{+}, reflecting their preferential association with the nucleosomal surface. To examine the effect of ion parameterization, RDFs were calculated using both the standard 12–6 and the m12–6–4 models. Although both models reproduced enhanced divalent ion localization relative to Na^{+}, they yielded distinct distribution profiles (Figure 1b; Supplementary Figure 1a). Notably, the m12–6–4 model produced a diminished first peak for Ca^{2+} at ~2.5 Å, consistent with reduced short-range overbinding, and a higher overall RDF magnitude for Mg^{2+}, indicative of stronger nucleosome association. These findings underscore the importance of ion parameter choice in accurately modeling ion–macromolecule interactions.

To further evaluate the accuracy of the ion models, we compared the simulated Ca^{2+}/Mg^{2+} binding ratios to

those reported in experimental studies[36]. Prior measurements have estimated that chromatin binds one Ca^{2+} ion per ~12.5–20 base pairs and one Mg^{2+} per ~20–30 base pairs, corresponding to ~7.4–11.8 Ca^{2+} and ~4.9–7.4 Mg^{2+} ions per nucleosome (147 bp), yielding an experimental Ca^{2+}/Mg^{2+} ratio of ~1.56[36]. From our simulations, we computed the number of divalent cations within 5 Å of the nucleosome. The 12–6 model yielded a binding ratio of 2.09, whereas the m12–6–4 model produced a ratio of 1.35, which is in closer agreement with experimental values (Supplementary Table 4).

In addition, previous experimental and simulation studies have shown that Ca^{2+} preferentially interacts with the DNA phosphate backbone, whereas Mg^{2+} exhibits stronger affinity for nucleobase sites, following the order major groove > phosphate backbone > minor groove[37,38]. In our simulations, the m12–6–4 model accurately reproduces this experimentally supported Mg^{2+} binding hierarchy, whereas the conventional 12–6 model substantially underestimates Mg^{2+} association with the major groove (Supplementary Figure 2). Similarly, for Ca^{2+}, the m12–6–4 parameterization yields DNA-binding patterns that are in good agreement with experimental observations.

We next examined the influence of water box size by increasing the minimum distance between the nucleosome and the periodic box edge to 30 Å and 50 Å (Simulation Sets 3 and 4; Supplementary Tables 2–3). As expected, water box size had negligible effects on the RDF profiles of divalent ions. The overall shapes and trends of the RDF curves remained highly consistent across box sizes, with Spearman correlation coefficients reaching 0.99 (Supplementary Figure 1). These results indicate that while box size affects ion counts, it does not substantially alter the relative distribution profiles of ions around the nucleosome.

To determine the most appropriate box size, we compared the Mg^{2+}/Na^{+} binding ratios from our simulations to an experimentally reported ratio of 2.75 for nucleosomes[18]. The standard box size considerably underestimated this ratio 0.74 (53 Mg^{2+} vs. 72 Na^{+} ions), whereas simulations using a 50 Å buffer produced a ratio of 1.34 (74 Mg^{2+} vs. 55 Na^{+}), in better agreement with experimental findings (Supplementary Table 5). The remaining discrepancy likely reflects differences in ion concentrations between the simulations and experimental conditions. Based on this improved correspondence, we adopted the larger box size (Simulation Set 4 in Supplementary Table 2) for all subsequent analyses involving full-length nucleosomes with histone tails.

Divalent cations exhibit distinct binding modes to the nucleosome

To elucidate how divalent cations interact with the nucleosome, we identified bound ions and characterized their binding patterns across distinct structural regions from simulations (Figure 2a). Specifically, we

quantified the regional binding preferences of Ca^{2+} and Mg^{2+} by calculating the average number of ions associated with predefined nucleosomal regions throughout the simulations (as defined in Supplementary Table 6). Both ions showed a strong propensity to bind nucleosomal DNA, accounting for approximately 61.4% (43 ions, Ca^{2+}) and 71.6% (53 ions, Mg^{2+}) of total binding events, respectively, highlighting the dominant role of electrostatics in mediating their interactions (Figure 2b).

Within the DNA-associated population (Figure 2c; Supplementary Table 7), Ca^{2+} exhibited a preference for the DNA backbone (31.4%, 22 ions), followed by the major (18.6%, 13 ions) and minor grooves (11.4%, 8 ions). In contrast, Mg^{2+} most frequently bound to the major groove (29.7%, 22 ions), followed by the backbone (25.7%, 19 ions) and minor groove (16.2%, 12 ions). Additionally, a fraction of both cations localized to the gap between the two gyres of nucleosomal DNA—termed gap binding—with 20% (14 ions) for Ca^{2+} and 13.5% (10 ions) for Mg^{2+} (Supplementary Movies 1 and 2). These binding preferences align with previous experimental and computational studies of DNA–ion interactions[37-39]. The observed differences likely reflect the distinct hydration characteristics of the two ions: Mg^{2+}, with its smaller ionic radius and tighter hydration shell, favors partially hydrated binding in the major groove, while the larger, less tightly hydrated Ca^{2+} more readily engages in direct contact with the DNA backbone[40-42].

For ions bound to histones (Figure 2c; Supplementary Table 7), both Ca^{2+} and Mg^{2+} predominantly associated with the histone core, comprising 15.7% (11 ions) and 12.2% (9 ions) of total binding events, respectively. Though less frequent, interactions with histone tails were also observed—2.9% (2 ions) for Ca^{2+} and 1.4% (1 ion) for Mg^{2+}. Despite their scarcity, such interactions may have functional implications in modulating histone tail dynamics, regulating the accessibility of post-translational modification sites, and facilitating inter-nucleosomal interactions. Interestingly, a significant fraction of both ions was localized at histone–DNA interfaces, accounting for 20% (14 ions, Ca^{2+}) and 14.9% (11 ions, Mg^{2+}).

We further identified the total number of stably bound ions from three independent simulation replicates, defined as ions maintaining persistent interactions for more than 50% of the trajectory in each replicate (Supplementary Table 8). Consistent with their overall binding patterns, Ca^{2+} preferentially associated with histones (67 Ca^{2+} vs. 37 Mg^{2+}), whereas Mg^{2+} predominantly bound DNA (58 Mg^{2+} vs. 14 Ca^{2+}). Within DNA, Mg^{2+} most frequently occupied the major groove (38 Mg^{2+} vs. 4 Ca^{2+}), followed by the backbone (9 Mg^{2+} vs. 6 Ca^{2+}) and minor groove (11 Mg^{2+} vs. 4 Ca^{2+}). In contrast, a larger fraction of Ca^{2+} ions was stably located in the DNA gap region (27 Ca^{2+} vs. 13 Mg^{2+}). Both cations also exhibited stable interactions with the histone core (42 Ca^{2+} vs. 31 Mg^{2+}), preferentially at acidic residues such as H2A D77 (loop L1) and H3 E41 (α1 helix), as well as the canonical acidic patch, which provide favorable electrostatic environments

for divalent ion coordination. These results establish a foundation for examining how stably bound divalent ions influence nucleosome structure and conformational dynamics in subsequent analyses.

Binding of divalent ions alters nucleosomal DNA gyre spacing

Given the extensive binding of divalent ions to the nucleosome, we next examined whether these ions influence the geometry and dynamics of nucleosomal DNA. To this end, we calculated a comprehensive set of DNA structural parameters, including six base pair parameters (shear, stretch, stagger, buckle, propeller twist, and opening), six base pair step parameters (roll, tilt, twist, slide, shift, and rise), as well as the widths of the major and minor grooves. These parameters were compared between nucleosomal DNA regions containing stably bound divalent ions and control simulations containing only monovalent ions.

Our analysis revealed that most base pair and step parameters remained largely unchanged upon divalent ion binding (Supplementary Figure 3). In terms of groove geometry, divalent ion binding induced a slight narrowing of the major groove, whereas the minor groove width remained essentially unaffected (Supplementary Figure 4). These findings are consistent with prior reports showing that Mg^{2+} minimally alters DNA groove dimensions, in contrast to its more pronounced structural effects on RNA folding and conformation[38,43].

Beyond local conformational changes, we further investigated whether divalent ion binding influences the higher-order spatial organization of nucleosomal DNA, particularly the gapping between DNA gyres. To this end, we quantified the inter-gyre spacing—defined as the distance between the upper and lower DNA gyres—across SHLs (Figure 3a; Supplementary Table 9). Given the frequent occurrence of divalent ion binding within the inter-gyre region, we hypothesized that such interactions may modulate nucleosomal DNA compaction.

In $NUC_{tailless}$ systems (Simulation Set 5), Mg^{2+} binding between the DNA gyres consistently reduced the gaping distance (Figure 3b). A similar compaction effect was observed in nucleosomes with intact histone tails, where both Mg^{2+} and Ca^{2+} binding led to decreased inter-gyre spacing, with Ca^{2+} exerting a more pronounced effect (Supplementary Figure 5a). This reduction in spacing is likely attributable to charge neutralization of the DNA phosphate backbone by divalent cations, thereby alleviating electrostatic repulsion between the gyres. To further quantify this effect, we computed electrostatic forces between the upper and lower gyre fragments across different SHLs. Specifically, we projected the electrostatic force vectors (with versus without divalent ions) onto the vector connecting the centroids of the two gyres. As shown in Figure 3c, the magnitude of this projected force was significantly reduced at multiple SHLs,

indicating that Mg^{2+} binding attenuates inter-gyre electrostatic repulsion and facilitates DNA gyre compaction.

Divalent ions modulate nucleosome plasticity and compaction

Nucleosomes exhibit considerable structural plasticity, which is essential for regulating DNA accessibility, chromatin architecture, and ultimately gene expression[32,44,45]. This plasticity is modulated by a variety of factors, including the incorporation of histone variants and PTMs[35]. Here, we investigated whether and how divalent ions affect nucleosome plasticity.

Using Simulation Set 5 on tailless nucleosomes, we calculated the Young's modulus in the presence and absence of Mg^{2+} by modeling the nucleosome as a homogeneous elastic cylinder (Figure 4a). Our results show that divalent ions significantly increase nucleosome stiffness: the Young's modulus increased from 10.39 ± 0.43 MPa under divalent ion-free conditions to 12.16 ± 0.55 MPa upon the addition of 15 mM Mg^{2+} (Figure 4b). To evaluate the generality of this effect, we also analyzed nucleosomes with intact histone tails in presence of 15 mM Mg^{2+} or Ca^{2+} (Simulation Set 4, NUC_{tail}). In these systems, both Mg^{2+} and Ca^{2+} increased the Young's modulus (Supplementary Figure 5b), indicating enhanced mechanical rigidity across nucleosomal states.

We next quantified changes in the vertical dimension (height) of the nucleosome core particle. Box plot analysis (Figure 4c) revealed that Mg^{2+} binding reduced nucleosome height, consistent with a more compact architecture. Nucleosome height and Young's modulus were moderately negatively correlated ($R = -0.43$; Figure 4d), suggesting that vertical compaction contributes to mechanical stiffening.

Further analysis of DNA dynamics revealed that Mg^{2+} binding enhanced anti-correlated motions within distinct regions of the DNA backbone (Figure 4e). Nucleotides around –30 to +30 (SHL –3 to +3) exhibited pronounced anti-correlated motions with nucleotides around +60 to +70 (SHL +6 to +7), consistent with decreased gaping distance between gyres. In addition, the diagonal elements of the cross-correlation map revealed an expanded range of strong self-correlations for nucleotides within the –30 to +30 region, indicating that these segments fluctuate more coherently. These long-range motions and enhanced local correlations likely underlie the observed increase in nucleosome stiffness and compaction.

Finally, we assessed whether divalent ion binding affects nucleosomal DNA unwrapping of tailless nucleosomes. Analyses of DNA radius of gyration (Rg) revealed a slightly decease of Rg of nucleosomal DNA (Supplementary Figure 6a). However, no significant differences were observed in DNA unwrapping or in the binding free energies between the histone octamer and DNA in the tailless nucleosome (Supplementary Figures 6b and 7). These observations indicate that the increased stiffness and compaction

arise primarily from reduced gyre spacing and altered nucleosome architecture, rather than changes in histone core–DNA binding affinity or DNA unwrapping dynamics.

Electrostatic screening by divalent ions weakens histone tail–DNA binding

In our simulations, divalent cations bind extensively to the DNA phosphate backbone, partially neutralizing its negative charge. This electrostatic screening is expected to modulate histone–DNA interactions and, consequently, nucleosome dynamics. To investigate this, we first analyzed the average number of contacts between DNA and either the histone core domain or histone tails.

Compared to ion-free systems, interactions between the histone core domain and DNA remained largely unaffected upon Ca^{2+} or Mg^{2+} binding (Supplementary Figure 8a). In contrast, histone tail–DNA contacts were significantly reduced in the presence of divalent cations (Supplementary Figure 8b), indicating that ion binding selectively disrupts electrostatic interactions mediated by the flexible histone tails. This was further corroborated by binding free energy calculations, which revealed a marked decrease in tail–DNA binding affinity (Supplementary Figures 8c and 8d).

To explore tail-specific effects, we quantified DNA contacts for individual histone tails (Figure 5a; Supplementary Figure 9). The H3, H4, and H2A-N tails exhibited the most frequent DNA contacts, with the H3 tail showing the greatest sensitivity to divalent cation binding. Free energy calculations confirmed a substantial decrease in H3 tail–DNA binding affinity in the presence of Ca^{2+} or Mg^{2+} (Figure 5b).

Residue-level analyses further revealed that divalent cations disrupt interactions primarily involving lysine and arginine residues within the histone tails (Figure 5c; Supplementary Figure 10). This effect was most pronounced for the H3 tail, particularly at residues R2, R8, and R17. While similar trends were observed for other tails, the magnitude was considerably smaller, highlighting the H3 tail's unique sensitivity to ionic screening.

To assess kinetic consequences, we analyzed histone tail conformational flexibility and residence time on nucleosomal DNA. Conformations of the H3 tail across three independent simulations revealed markedly increased flexibility in the presence of Ca^{2+} or Mg^{2+} (Figure 5d and Supplementary Figure 11; Supplementary Movies 3–5). Quantification of residence times and binding events revealed that divalent cations significantly reduced histone tail–DNA binding durations (Figure 5e and 5f; Supplementary Figures 12 and 13). For instance, the H3 tail's mean residence time decreased by ~41% in the presence of Mg^{2+} (from 336 ns to 199 ns; Figure 5e). These effects were most pronounced for the H3 tail, followed by H4, consistent with contact-based observations (Supplementary Figure 12). Notably, the number of H3 tail–DNA binding events increased in divalent ion conditions, suggesting more frequent but transient

interactions, indicative of enhanced tail dynamics (Figure 5f).

Discussion

Our study provides an atomistic perspective on how divalent cations regulate nucleosome structure and dynamics. Through extensive all-atom MD simulations totaling over 80 microseconds, we demonstrate that Ca^{2+} and Mg^{2+} ions exhibit preferential and selective binding to both nucleosomal DNA and histone proteins, leading to distinct structural and mechanical consequences. These ions not only alleviate electrostatic repulsion between DNA gyres, resulting in tighter DNA wrapping and increased mechanical rigidity, but also modulate the flexibility and DNA-binding behavior of histone tails—jointly shaping nucleosome plasticity and accessibility (Figure 6).

A key finding from our work is that divalent cations promote DNA gyre compaction by stabilizing conformations with reduced inter-gyre spacing. This compaction is primarily driven by charge neutralization of the DNA phosphate backbone, which decreases electrostatic repulsion between adjacent DNA gyres. The resulting structural change is associated with a measurable decrease in nucleosome height and a pronounced increase in mechanical stiffness, supporting the view that divalent ions serve to rigidify the nucleosome and reduce its structural plasticity.

Nucleosome plasticity has recently emerged as a crucial factor in chromatin phase behavior, including its role in facilitating LLPS and supporting multivalent interactions between nucleosomes[32]. Notably, recent work has shown that even a single histone variant can encode distinct mechanical properties within its nucleosome: CENP-A–containing nucleosomes are more elastic than canonical H3 nucleosomes, whereas CENP-C—the essential CENP-A–binding protein—can further stiffen CENP-A nucleosomes in vitro[35]. These findings highlight the importance of histone composition and associated factors in preserving the mechanical properties of centromeric chromatin.

In this work, our atomistic simulations further demonstrate that divalent ions modulate the intrinsic mechanical properties of individual nucleosomes, identifying Mg^{2+} and Ca^{2+} as extrinsic, tunable regulators of nucleosome stiffness. This highlights an underappreciated mechanism by which local ionic environments may influence chromatin accessibility, transcriptional output, and epigenetic signaling. Our findings are consistent with previous studies showing that divalent ions stiffen and compact chromatin fibers and act synergistically with linker histones[4,7]. Collectively, these observations suggest that mechanical changes at the nucleosome level may synergistically regulate the mechanics and physical state of chromatin fibers; however, their impact on the strength and dynamics of inter-nucleosomal interactions warrants further investigation.

In parallel, we observed that divalent cations significantly modulate the conformational dynamics of histone tails. Both Mg^{2+} and Ca^{2+} reduce the persistence of tail–DNA interactions and enhance tail mobility, particularly in specific regions of the H3 tail. Because histone tails serve as hotspots for post-translational modifications (PTMs) and key binding interfaces for chromatin-associated proteins, such ion-dependent modulation of tail dynamics may profoundly influence nucleosome recognition and regulatory crosstalk. For example, increased tail accessibility may facilitate recruitment of chromatin regulators such as Heterochromatin Protein 1 (HP1), promoting heterochromatin formation and stabilizing higher-order chromatin structures[46]. These observations are consistent with and extend previous computational and experimental studies showing that tail–DNA interactions govern nucleosome recognition by reader domains and affect higher-order chromatin folding[25,47-50].

Histone tails are essential contributors to higher-order chromatin folding, self-association, and compaction. Notably, even high concentrations of divalent cations are insufficient to induce self-association of nucleosomal arrays in the absence of histone tails[51,52]. Our simulations reveal that divalent cations "unlock" histone tails, significantly reducing tail–DNA interactions within individual nucleosomes. These decreases in intra-nucleosome tail–DNA contacts, coupled with enhanced tail dynamics, may facilitate interactions between histone tails and neighboring nucleosomes, promoting both tail–DNA and tail–tail inter-nucleosomal binding. Consistent with this, recent atomistic simulations of tri-nucleosome systems have shown that histone tails mediate chromatin compaction via tail–DNA and tail–tail interactions[53].

Beyond local regulation of individual nucleosomes, divalent cations play essential roles in shaping chromatin organization within physiologically variable ionic environments. Nuclear compartments such as the nucleolus and heterochromatin domains are enriched in Mg^{2+} and Ca^{2+}, potentially leading to distinct nucleosome structural dynamics and chromatin states[12,35]. Our findings thus provide a molecular framework connecting altered divalent ion fluxes to genome structural changes in health and disease. Moreover, nuclear divalent cation levels are not static but actively modulated by metabolic signals. For example, transient increases in nuclear ATP observed during hormone stimulation can promote chromatin opening by chelating free Mg^{2+} ions, while subsequent ATP hydrolysis releases Mg^{2+} to trigger chromatin re-condensation[22-24]. This dynamic ATP–Mg^{2+} cycling may establish a defined temporal window of transcriptional accessibility through phase separation mechanisms, effectively linking cellular energy status to chromatin structural transitions. Together, these insights highlight the critical role of divalent cations in coordinating chromatin mechanics, epigenetic regulation, and cellular responses to changing physiological and pathological ionic microenvironments.

One major limitation of this study is that the effects of divalent ions were examined at the single-nucleosome level, due to the computational challenges of simulating extremely large systems such as chromatin fibers at full atomic resolution. While coarse-grained models are powerful tools for investigating higher-order chromatin organization, their simplified representations of nucleosomes make it difficult to accurately capture specific divalent-ion interactions. Future efforts integrating multiscale computational approaches with experimental techniques will be essential to determine how the divalent-ion–induced effects observed at the single-nucleosome level regulate inter-nucleosome interactions and higher-order chromatin structure. Nevertheless, our findings provide a mechanistic foundation for understanding how divalent ions may influence chromatin behavior through their direct effects on individual nucleosomes.

Our understanding of how divalent ions influence nucleosome thermal stability remains incomplete, and there is still debate over whether these ions suppress or promote nucleosome wrapping[21,54,55]. In our simulations, although we observed a significant decrease in tail–DNA interactions, no appreciable changes were detected in histone core–DNA binding or DNA unwrapping. This is likely due in part to our use of the Widom 601 DNA sequence, which forms exceptionally stable nucleosomes, even in the absence of histone tails. These factors may limit our ability to capture large-scale unwrapping events or ion-dependent modulation of DNA unwrapping. Future studies should consider employing different native DNA sequences and explicitly incorporating linker DNA to more comprehensively evaluate how divalent ions modulate nucleosome thermodynamic stability and the coupling between divalent ion–binding events and DNA-unwrapping processes.

In addition to Mg^{2+} and Ca^{2+}, redox-active transition metals such as Cu^{2+}/Cu^{+} may play important biological roles by modulating DNA conformation, histone oxidation, and chromatin remodeling[56,57]. Recent studies indicate that Cu^{2+} binds mononucleosomes with salt-dependent affinity, interacting with both the DNA phosphate backbone and nucleobases, and inducing measurable DNA conformational distortions[58,59]. Modeling these effects could provide valuable insights into copper-induced oxidative DNA damage and its potential implications in disease processes, including cancer.

In summary, our study provides a mechanistic framework for understanding how divalent ions dynamically tune nucleosome structure, histone tail accessibility, and chromatin regulatory potential. These insights pave the way for future experimental investigations using ion-sensitive cryo-EM, NMR spectroscopy, and single-molecule force measurements. Extending this framework to nucleosome arrays and in the presence of chromatin-binding factors will be essential for elucidating how localized ionic microenvironments influence genome function at the systems level.

Methods

Construction of nucleosome models

We constructed homotypic human nucleosome structural models based on the high-resolution X-ray crystal structure of the nucleosome core particle (PDB ID: 1KX5). The Widom 601 DNA sequence was incorporated into the 1KX5 structure using the 3DNA program[60], and the histone sequences were replaced with the corresponding human histones (see Supplementary Table 1 for sequence details), following the same sequence set used in our recent work[61].

To generate the tailless nucleosome model ($NUC_{tailless}$), the histone tails were truncated at the following residues: K37 (H3), K20 (H4), A13 (H2A) and K118 (H2A), and K26 (H2B). The full-tail model (NUC_{tail}) was subsequently reconstructed by extending the polypeptide backbone from the truncation sites using standard dihedral angles ($\Phi = -60°$, $\Psi = 30°$), with the tails symmetrically oriented into the solvent. Thus, two nucleosome models—NUC_{tail} and $NUC_{tailless}$—were constructed for subsequent MD simulations.

Choice of force fields, water models, and ion parameters for simulations

Accurately simulating highly charged macromolecular systems such as the nucleosome requires careful selection of the force field, water model, and ion parameters. These choices are critical for reliably modeling protein–DNA interactions, capturing the conformational dynamics of intrinsically disordered histone tails, and representing interactions among the nucleosome, solvent, and ions.

In our simulations, we employed the AMBER ff14SB force field for proteins[62] and the OL15 force field for nucleic acids[63]. Both have been widely used in nucleosome MD simulations, supporting their reliability and robustness[25,64-67]. Water molecules were modeled using the TIP4PEW model[68], and monovalent ions were described using the conventional 12-6 Lennard-Jones (LJ) nonbonded potential[69].

For divalent ions, a more nuanced approach was required. Although the 12–6 LJ potential is widely used due to its simple functional form and computational efficiency, it fails to accurately reproduce experimental properties of divalent ions for highly charged systems[70,71]. This is primarily because it underestimates the interactions between metal ions and surrounding water molecules, and it inherently neglects polarization effects[70].

To overcome these limitations, Li et al. introduced a modified nonbonded model known as the 12–6–4 LJ-type potential[71-73], which adds a 1/r term to the standard 12–6 formulation to account for ion-induced dipole interactions. This refinement significantly improves agreement with experimental values for hydration free energies (HFE), ion–oxygen distances (IOD), and coordination numbers (CN)[71-73]. Building on this work,

Panteva et al. further refined the 12–6–4 model (m12–6–4) by adjusting specific pairwise parameters to better reproduce site-specific binding free energies of divalent ions with nucleic acid moieties such as dimethyl phosphate, adenosine, and guanosine[74]. These refinements have proven effective in accurately modeling metal ion binding to nucleic acids and have been successfully applied to simulations involving protein–nucleic acid interactions[75-78].

To evaluate the influence of different ion models in our study, we parameterized divalent ions using both the standard 12–6 and the refined m12–6–4 models, allowing for a direct comparison of their impact on simulation outcomes.

MD simulation protocol

Five sets of MD simulations were performed to systematically investigate the binding of Ca^{2+} and Mg^{2+} ions to the nucleosome and to assess the impact of ion parameterization on simulation outcomes, resulting in a total of 48 independent trajectories and 81 μs of aggregate simulation time (see Supplementary Tables 2 and 3 for details).

First, the full nucleosome models (NUC_{tail}) were solvated in a periodic water box, ensuring a minimum distance of 5 Å between any nucleosome atom and the box edges. To mimic physiological ionic strength, NaCl was added to achieve a final concentration of 150 mM. Divalent ion concentrations were determined based on experimentally measured values in mitotic chromosomes, where Ca^{2+} concentrations range from 20–32 mM and Mg^{2+} from 12–22 mM[36]. Specifically, we selected the minimum and median values within these ranges for use in our simulations (see Supplementary Tables 2 and 3 for details). In Simulation Set 1, Mg^{2+} and Ca^{2+} ions were parameterized using the m12–6–4 model and added separately to the system. For each ion condition, three independent replicates were performed to ensure statistical robustness. To examine the effects of ion parameterization, Simulation Set 2 was carried out using identical system setups, but with Mg^{2+} and Ca^{2+} ions described by the conventional 12–6 model.

Since the size of the water box directly determines the total number of ions present in the simulation system, we performed additional simulations to evaluate the influence of water box dimensions on simulation outcomes. Specifically, we used the m12–6–4 parameter set for divalent ions and increased the minimum distance between the nucleosome and the periodic box boundary to 30 Å and 50 Å, respectively. These simulations are referred to as Simulation Set 3 and Simulation Set 4.

Finally, to investigate the impact of divalent ions on the mechanical properties and dynamics of nucleosomal DNA, particularly DNA unwrapping, we simulated the tailless nucleosome model ($NUC_{tailless}$). The

absence of histone tails allowed for longer timescale simulations, facilitating the observation of potential unwrapping events. This setup is referred to as Simulation Set 5.

All MD simulations were performed using the AMBER 22 software package[79]. Each system underwent a two-stage energy minimization: 10,000 steps of steepest descent followed by 10,000 steps of conjugate gradient minimization. The systems were then gradually heated from 100 K to 310 K over 200 ps in the canonical ensemble (NVT), followed by 2ns of equilibration in the isothermal-isobaric ensemble (NPT). Production simulations were conducted in the NPT ensemble at 310 K, regulated by Langevin dynamics with a collision frequency $\gamma = 2$ ps^{-1}, and at 1 atm pressure, maintained using the Berendsen barostat[80,81]. Non-bonded interactions were truncated at 10 Å, and long-range electrostatics were calculated using the Particle Mesh Ewald (PME) method[82]. Periodic boundary conditions were applied throughout, and all bond lengths involving hydrogen atoms were constrained using the SHAKE algorithm[83]. All simulations were independently repeated three times, and coordinates of the solutes were saved every 100 ps for Simulation Sets 1, 2, and 5, and every 40 ps for Simulation Sets 3 and 4.

Analysis of MD simulation trajectories

Trajectory visualization and analysis were performed using VMD[84], a set of TCL scripts and custom Python scripts, and AMBER Tools[79]. The initial 100 ns of each 500 ns trajectory and the first 200 ns of each 10,000 ns trajectory were discarded to allow for conformational equilibration. Unless otherwise noted, all analyses were performed at 1 ns intervals for the relevant simulation sets. To characterize ion distributions around the nucleosome, we computed RDFs using the radial command in *cpptraj* (AMBER Tools) [79]. The reference density (ρ) was defined as the ratio of the total number of ions to the average system volume, using the volume *keyword*.

Histone-DNA interactions were assessed by calculating the mean number of atomic contacts between DNA and histone residues using TCL scripts. Atomic contacts were defined as any pair of non-hydrogen atoms (one from DNA and one from histone) within 4 Å. Histone–DNA contacts were analyzed from trajectory frames extracted every 400 ps for Simulation Set 4 and every 1 ns for Simulation Set 5. Binding free energies between histones and DNA were estimated using the molecular mechanics/generalized Born surface area (MM/GBSA) approach implemented in AMBER 22 package[79]. MM/GBSA calculations were performed at 1 ns intervals for Simulation Sets 4, and at 10 ns intervals for Simulation Set 5.

To investigate histone tail–DNA binding dynamics, we calculated residence times by identifying binding events, defined as frames in which at least 10% of histone tail residues were in contact with DNA. The

residence time was defined as the continuous duration of each binding event. To ensure statistical significance, only binding events lasting longer than 10 ns were included in the final analysis.

Classification of divalent ion binding modes to the nucleosome

We defined distinct ion binding regions and categorized the bound ions into seven binding modes within 5 Å of the nucleosome. Four of these modes involve interactions with DNA: DNA backbone binding, major groove binding, minor groove binding, and DNA gap binding. Two modes correspond to interactions with histone: histone tail binding and histone core binding. The final mode, DNA-histone interface binding, includes ions located at the interface between DNA and histone. Detailed definitions and classification criteria for each binding mode are provided in Supplementary Table 6.

To systematically characterize the stable binding behavior of divalent ions in nucleosome simulations, we identified stably bound ions as those maintaining contact with at least one atom or residue in a predefined binding region for more than 50% of the total simulation time in a single trajectory, regardless of whether the contact is continuous. The number of bound and stably bound divalent ions in each binding mode was quantified using custom Python scripts. For each system, the average number of bound ions was first averaged over all frames in each run, and then averaged across three independent runs.

Structural and mechanical analysis of nucleosomal DNA

To investigate whether divalent ion binding induces structural alterations in nucleosomal DNA, we first analyzed local DNA conformational changes at ion-binding sites. DNA geometrical parameters were calculated using AMBER Tools[79], including six base pair parameters (shear, stretch, stagger, buckle, propeller, and opening), six base pair step parameters (roll, tilt, twist, slide, shift, and rise), as well as major and minor groove widths.

To assess global structural changes, we calculated the gaping distances between the two DNA gyres of the nucleosome at superhelical locations (SHLs) ±4, ±5, and ±6 (Figure 3a). Each gaping distance was defined as the distance between the centroids of two 3-bp DNA segments located on the upper and lower gyres of the nucleosome. For SHL ±4, the distance was calculated between SHL –4 and SHL +4. For SHL ±5, two asymmetric SHL pairs were analyzed: SHL –5/+3 and SHL –3/+5. Similarly, for SHL ±6, distances were measured between SHL –6/+2 and SHL –2/+6. The exact base pair ranges corresponding to each 3-bp segment are listed in Supplementary Table 9.

Nucleosome unwrapping events were identified using custom Python scripts, in which unwrapping was defined as any base pair deviating more than 7 Å from its initial central position at 10 ns intervals.

Additionally, the Rg of the nucleosomal DNA was calculated to assess changes in overall DNA compactness. Finally, to probe how divalent ions influence coordinated DNA motions, we generated dynamic cross-correlation matrices (DCCMs) for phosphate atoms of a single DNA strand in tailless nucleosomes using the Bio3D package in R[85].

To assess whether divalent ion binding influences the mechanical rigidity of the nucleosome, we adopted a previously established method to estimate the Young's modulus of the nucleosome[86]. In this approach, the nucleosome is modeled as a homogeneous elastic cylinder (Figure4a; Supplementary Figure 14), whose boundaries are defined based on the root mean square fluctuations (RMSF) of phosphorus (P) atoms from the DNA and Cα atoms from the histones. Simulation trajectories were divided into segments of 20 frames, and the RMSF of P and Cα atoms was calculated for each segment. To minimize bias from highly flexible regions, ten atoms per segment with RMSF values exceeding 0.6 Å were excluded along each dimension (height and radius). For each segment, the height and radius of the elastic cylinder were then determined. The mean and variance of these dimensions across all frames were subsequently used to calculate the Young's modulus using the following equation:

$$E=\frac{k_b T(1-\nu-2\nu^2)}{V(\varepsilon_{zz}^2-\nu\varepsilon_{zz}^2+2\varepsilon_{rr}^2+4\nu\varepsilon_{zz}\varepsilon_{rr})} \quad (1)$$

,where k_b is the Boltzmann constant and T is the simulation temperature 310 K. V is the volume of cylinder calculated from the mean radius and height of the structure. The strain components ε_{zz} and ε_{rr} represent height and radial strains, respectively. ν is the Poisson's ratio.

Analyses were performed at 40 ps intervals for *Simulation Set 4* and 100 ps intervals for Simulation Set 5. Each trajectory in *Simulation Set 5* was divided into 400-ns segments (spanning 200 ns to 9800 ns), and the mean Young's modulus across all segments was reported. Segments exhibiting clear DNA unwrapping were excluded from the analysis; for the 15 mM Mg^{2+} system, only the intervals 3400–4600 ns and 7800–8200 ns in the second of the three independent replicates were omitted, whereas all segments were retained for the 150 mM NaCl system.

Poisson's ratio (ν) describes the lateral deformation of a material under axial stress. For isotropic elastic materials, ν theoretically ranges from 0 to 0.5, with values near 0 corresponding to highly compressible materials and $\nu = 0.5$ representing an incompressible limit. In this study, we set $\nu = 0.4$, consistent with the value used in previous studies [86,87]. To evaluate the sensitivity of the calculated Young's modulus to this parameter, we varied ν across 0.1, 0.2, 0.3, and 0.49 (Supplementary Figure 15). Although the absolute

modulus values changed as *v* varied, the overall monotonic trend remained unchanged, confirming that our main conclusions are robust with respect to reasonable variations in Poisson's ratio.

Electrostatic force calculations of nucleosome structures

Electrostatic forces between the upper and lower DNA gyre fragments were calculated at SHL positions ±4, ±5, and ±6, using the same fragment definitions as in the gaping distance analysis. The electrostatic interactions were evaluated using DelphiForce, a computational tool that determines the magnitude and direction of electrostatic forces by computing the negative gradient of electrostatic potential[88]. This approach employs the finite difference method to solve the Poisson–Boltzmann equation, yielding the electrostatic potential $\Phi(r)$ at each grid point (i, j, k), represented as $\Phi(i, j, k)$. The electrostatic force components, denoted as $E(i, j, k)$, are then derived using finite difference approximations based on the spatial gradients of the potential in the x, y, and z directions,

$$E_x(i,j,k) = -\frac{[\Phi(i,j,k) - \Phi(i-1,j,k)]}{h}, \quad (2)$$

$$E_y(i,j,k) = -\frac{[\Phi(i,j,k) - \Phi(i,j-1,k)]}{h}, \quad (3)$$

$$E_z(i,j,k) = -\frac{[\Phi(i,j,k) - \Phi(i,j,k-1)]}{h} \quad (4)$$

,where i, j, and k are the indices of the grid points, and h refers to the spacing between adjacent grid points.

Statistics and Reproducibility

All quantitative analyses were based on three independent MD simulations. For each condition, three independent simulation replicates were performed. Time-averaged quantities were first averaged over time within each trajectory after equilibration, and then averaged across independent replicates. Error bars represent the standard error of the mean (SEM) calculated across replicates. For box plots, values represent distributions obtained by pooling time-averaged data from each independent simulation replicate.

For event-based analyses, including residence times, binding events, and representative conformations, data were aggregated across the three independent simulation replicates, accounting for both histone tails in each nucleosome. Statistical comparisons between conditions were performed using two-sided Welch's t-tests, with exact p-values and effect sizes (Cohen's d) reported where applicable.

Reproducibility was ensured by performing all simulations using identical protocols, applying the same analysis pipelines to all independent trajectories, and repeating analyses across the independent replicates.

All data files, analysis scripts, and parameters used for simulations are provided to ensure computational reproducibility.

Data availability

All simulation parameter files, MD trajectories underlying the figures are available from the Zenodo repository at (https://doi.org/10.5281/zenodo.18232757)[89]. Processed data used to generate the figures and statistical analyses are included in the same repository. All other data supporting the findings of this study are available from the corresponding author upon reasonable request.

Code availability

All custom analysis scripts used in this study are available from the Zenodo repository at (https://doi.org/10.5281/zenodo.18232757)[89]. DNA geometry and dynamics were analyzed using AMBER Tools 22 and Bio3D (v2.4.5). Electrostatic analyses were performed using DelPhiForce. Molecular visualization and trajectory inspection were performed using VMD (v1.9.4a) and UCSF Chimera (v1.17.3).

References

1 Almassalha, L. M. *et al.* Chromatin conformation, gene transcription, and nucleosome remodeling as an emergent system. *Sci. Adv.* **11**, eadq6652, doi:10.1126/sciadv.adq6652 (2025).

2 Phengchat, R. *et al.* Calcium ions function as a booster of chromosome condensation. *Sci. Rep.* **6**, 38281, doi:10.1038/srep38281 (2016).

3 Hansen, J. C., Maeshima, K. & Hendzel, M. J. The solid and liquid states of chromatin. *Epigenetics Chromatin* **14**, 50, doi:10.1186/s13072-021-00424-5 (2021).

4 Lin, X. & Zhang, B. Explicit ion modeling predicts physicochemical interactions for chromatin organization. *eLife* **12**, RP90073, doi:10.7554/eLife.90073 (2024).

5 Korolev, N., Vorontsova, O. V. & Nordenskiöld, L. Physicochemical analysis of electrostatic foundation for DNA–protein interactions in chromatin transformations. *Prog. Biophys. Mol. Biol.* **95**, 23–49, doi:https://doi.org/10.1016/j.pbiomolbio.2006.11.003 (2007).

6 Bloomfield, V. A. DNA condensation. *Curr. Opin. Struct. Biol.* **6**, 334–341, doi:https://doi.org/10.1016/S0959-440X(96)80052-2 (1996).

7 Collepardo-Guevara, R. & Schlick, T. Crucial role of dynamic linker histone binding and divalent ions for DNA accessibility and gene regulation revealed by mesoscale modeling of oligonucleosomes. *Nucleic Acids Res.* **40**, 8803–8817, doi:10.1093/nar/gks600 (2012).

8 Visvanathan, A. *et al.* Modulation of Higher Order Chromatin Conformation in Mammalian Cell Nuclei Can Be Mediated by Polyamines and Divalent Cations. *PLoS ONE* **8**, e67689, doi:10.1371/journal.pone.0067689 (2013).

9 Vashishtha, A. K., Wang, J. & Konigsberg, W. H. Different Divalent Cations Alter the Kinetics and Fidelity of DNA Polymerases. *J. Biol. Chem.* **291**, 20869–20875, doi:10.1074/jbc.R116.742494 (2016).

10 Sukhanova, M. V., Anarbaev, R. O., Maltseva, E. A., Kutuzov, M. M. & Lavrik, O. I. Divalent and multivalent

cations control liquid-like assembly of poly(ADP-ribosyl)ated PARP1 into multimolecular associates in vitro. *Commun. Biol.* **7**, 1148, doi:10.1038/s42003-024-06811-4 (2024).

11 Berridge, M. J., Bootman, M. D. & Roderick, H. L. Calcium signalling: dynamics, homeostasis and remodelling. *Nat. Rev. Mol. Cell Biol.* **4**, 517–529, doi:10.1038/nrm1155 (2003).

12 Hartwig, A. Role of magnesium in genomic stability. *Mutat. Res.* **475**, 113–121, doi:10.1016/s0027-5107(01)00074-4 (2001).

13 Ohyama, T. New Aspects of Magnesium Function: A Key Regulator in Nucleosome Self-Assembly, Chromatin Folding and Phase Separation. *Int. J. Mol. Sci.* **20**, 4232, doi:10.3390/ijms20174232 (2019).

14 McGinty, R. K. & Tan, S. Principles of nucleosome recognition by chromatin factors and enzymes. *Curr. Opin. Struct. Biol.* **71**, 16–26, doi:10.1016/j.sbi.2021.05.006 (2021).

15 Zhou, K., Gaullier, G. & Luger, K. Nucleosome structure and dynamics are coming of age. *Nat. Struct. Mol. Biol.* **26**, 3–13, doi:10.1038/s41594-018-0166-x (2019).

16 Zhang, H. *et al.* Electrostatic interactions in nucleosome and higher-order structures are regulated by protonation state of histone ionizable residue. *J. Chem. Phys.* **162**, 105101, doi:10.1063/5.0252788 (2025).

17 Park, S. *et al.* Native nucleosomes intrinsically encode genome organization principles. *Nature* **643**, 572–581, doi:10.1038/s41586-025-08971-7 (2025).

18 Gebala, M., Johnson, S. L., Narlikar, G. J. & Herschlag, D. Ion counting demonstrates a high electrostatic field generated by the nucleosome. *eLife* **8**, e44993 (2019).

19 Davey, C. A. & Richmond, T. J. DNA-dependent divalent cation binding in the nucleosome core particle. *Proc. Natl. Acad. Sci. U. S. A.* **99**, 11169–11174, doi:10.1073/pnas.172271399 (2002).

20 Nap, R. J. *et al.* The impact of charge regulation and ionic intranuclear environment on the nucleosome core particle. *J. Chem. Phys.* **161**, 235101, doi:10.1063/5.0241529 (2024).

21 Yang, Z. & Hayes, J. J. The divalent cations Ca2+ and Mg2+ play specific roles in stabilizing histone-DNA interactions within nucleosomes that are partially redundant with the core histone tail domains. *Biochemistry (Mosc.)* **50**, 9973–9981, doi:10.1021/bi201377x (2011).

22 Wright, R. H. G., Le Dily, F. & Beato, M. ATP, Mg2+, Nuclear Phase Separation, and Genome Accessibility. *Trends Biochem. Sci.* **44**, 565–574, doi:https://doi.org/10.1016/j.tibs.2019.03.001 (2019).

23 Grubbs, R. D. Intracellular magnesium and magnesium buffering. *Biometals* **15**, 251–259, doi:10.1023/a:1016026831789 (2002).

24 Maeshima, K. *et al.* A Transient Rise in Free Mg(2+) Ions Released from ATP-Mg Hydrolysis Contributes to Mitotic Chromosome Condensation. *Curr. Biol.* **28**, 444–451.e446, doi:10.1016/j.cub.2017.12.035 (2018).

25 Peng, Y., Li, S., Onufriev, A., Landsman, D. & Panchenko, A. R. Binding of regulatory proteins to nucleosomes is modulated by dynamic histone tails. *Nat. Commun.* **12**, 5280, doi:10.1038/s41467-021-25568-6 (2021).

26 Patel, R., Onyema, A., Tang, P. K. & Loverde, S. M. Conformational Dynamics of the Nucleosomal Histone H2B Tails Revealed by Molecular Dynamics Simulations. *J. Chem. Inf. Model.* **64**, 4709–4726, doi:10.1021/acs.jcim.4c00059 (2024).

27 Erler, J. *et al.* The role of histone tails in the nucleosome: a computational study. *Biophys J* **107**, 2911-2922, doi:10.1016/j.bpj.2014.10.065 (2014).

28 Patel, R. & Loverde, S. M. Unveiling the Conformational Dynamics of the Histone Tails Using Markov State Modeling. *J Chem Theory Comput* **21**, 4921-4938, doi:10.1021/acs.jctc.5c00196 (2025).

29 Grigoryev, S. A., Arya, G., Correll, S., Woodcock, C. L. & Schlick, T. Evidence for heteromorphic chromatin fibers from analysis of nucleosome interactions. *Proc. Natl. Acad. Sci. U. S. A.* **106**, 13317–13322, doi:10.1073/pnas.0903280106 (2009).

30 Correll, S. J., Schubert, M. H. & Grigoryev, S. A. Short nucleosome repeats impose rotational modulations on chromatin fibre folding. *EMBO J.* **31**, 2416–2426, doi:10.1038/emboj.2012.80 (2012).

31 Allahverdi, A., Chen, Q., Korolev, N. & Nordenskiöld, L. Chromatin compaction under mixed salt conditions: Opposite effects of sodium and potassium ions on nucleosome array folding. *Sci. Rep.* **5**, 8512, doi:10.1038/srep08512 (2015).

32 Farr, S. E., Woods, E. J., Joseph, J. A., Garaizar, A. & Collepardo-Guevara, R. Nucleosome plasticity is a critical element of chromatin liquid–liquid phase separation and multivalent nucleosome interactions. *Nat. Commun.* **12**, 2883, doi:10.1038/s41467-021-23090-3 (2021).

33 Chen, P., Li, G. & Li, W. Nucleosome Dynamics Derived at the Single-Molecule Level Bridges Its Structures and Functions. *JACS Au* **4**, 866–876, doi:10.1021/jacsau.3c00658 (2024).

34 Armeev, G. A., Kniazeva, A. S., Komarova, G. A., Kirpichnikov, M. P. & Shaytan, A. K. Histone dynamics mediate DNA unwrapping and sliding in nucleosomes. *Nat. Commun.* **12**, 2387 (2021).

35 Melters, D. P. *et al.* Intrinsic elasticity of nucleosomes is encoded by histone variants and calibrated by their binding partners. *Proc. Natl. Acad. Sci. U. S. A.* **116**, 24066–24074, doi:10.1073/pnas.1911880116 (2019).

36 Strick, R., Strissel, P. L., Gavrilov, K. & Levi-Setti, R. Cation-chromatin binding as shown by ion microscopy is essential for the structural integrity of chromosomes. *J. Cell Biol.* **155**, 899–910, doi:10.1083/jcb.200105026 (2001).

37 Ahmad, R., Arakawa, H. & Tajmir-Riahi, H. A. A Comparative Study of DNA Complexation with Mg(II) and Ca(II) in Aqueous Solution: Major and Minor Grooves Bindings. *Biophys. J.* **84**, 2460–2466, doi:https://doi.org/10.1016/S0006-3495(03)75050-4 (2003).

38 Fu, H. *et al.* Opposite effects of high-valent cations on the elasticities of DNA and RNA duplexes revealed by magnetic tweezers. *Phys. Rev. Lett.* **124**, 058101 (2020).

39 Xi, K., Wang, F.-H., Xiong, G., Zhang, Z.-L. & Tan, Z.-J. Competitive binding of Mg2+ and Na+ ions to nucleic acids: from helices to tertiary structures. *Biophys. J.* **114**, 1776–1790 (2018).

40 Bai, Y. *et al.* Quantitative and Comprehensive Decomposition of the Ion Atmosphere around Nucleic Acids. *J. Am. Chem. Soc.* **129**, 14981–14988, doi:10.1021/ja075020g (2007).

41 Long, M. P., Alland, S., Martin, M. E. & Isborn, C. M. Molecular dynamics simulations of alkaline earth metal ions binding to DNA reveal ion size and hydration effects. *Phys. Chem. Chem. Phys.* **22**, 5584–5596, doi:10.1039/c9cp06844a (2020).

42 Xu, H.-T., Zhang, N., Li, M.-R. & Zhang, F.-S. Comparison of the ionic effects of Ca2+ and Mg2+ on nucleic acids in liquids. *J. Mol. Liq.* **344**, 117781, doi:https://doi.org/10.1016/j.molliq.2021.117781 (2021).

43 Sharma, A. & Mishra, R. K. A brief study of the effects of magnesium divalent ions on the Dickerson DNA sequence at varying molar concentrations. *Eur. Phys. J. Plus* **140**, 60, doi:10.1140/epjp/s13360-025-06000-0 (2025).

44 Singh, H. R., Murawska, M. & Ladurner, A. G. Remodelers tap into nucleosome plasticity. *Nat. Struct. Mol. Biol.* **24**, 341–343, doi:10.1038/nsmb.3394 (2017).

45 Nocetti, N. & Whitehouse, I. Nucleosome repositioning underlies dynamic gene expression. *Genes Dev.* **30**, 660–672, doi:10.1101/gad.274910.115 (2016).

46 Watanabe, S., Mishima, Y., Shimizu, M., Suetake, I. & Takada, S. Interactions of HP1 Bound to H3K9me3 Dinucleosome by Molecular Simulations and Biochemical Assays. *Biophys. J.* **114**, 2336–2351, doi:10.1016/j.bpj.2018.03.025 (2018).

47 Peng, Y., Li, S., Landsman, D. & Panchenko, A. R. Histone tails as signaling antennas of chromatin. *Curr. Opin. Struct. Biol.* **67**, 153–160, doi:10.1016/j.sbi.2020.10.018 (2021).

48 Ghoneim, M., Fuchs, H. A. & Musselman, C. A. Histone Tail Conformations: A Fuzzy Affair with DNA. *Trends Biochem Sci.* **46**, 564–578, doi:10.1016/j.tibs.2020.12.012 (2021).

49 Morrison, E. A., Baweja, L., Poirier, M. G., Wereszczynski, J. & Musselman, C. A. Nucleosome composition regulates the histone H3 tail conformational ensemble and accessibility. *Nucleic Acids Res.* **49**, 4750–4767, doi:10.1093/nar/gkab246 (2021).

50 Zhou, B. R. *et al.* Histone H4 K16Q mutation, an acetylation mimic, causes structural disorder of its N-terminal basic patch in the nucleosome. *J. Mol. Biol.* **421**, 30–37, doi:10.1016/j.jmb.2012.04.032 (2012).

51 Schwarz, P. M., Felthauser, A., Fletcher, T. M. & Hansen, J. C. Reversible Oligonucleosome Self-Association: Dependence on Divalent Cations and Core Histone Tail Domains. *Biochemistry (Mosc.)* **35**, 4009–4015, doi:10.1021/bi9525684 (1996).

52 Gordon, F., Luger, K. & Hansen, J. C. The core histone N-terminal tail domains function independently and additively during salt-dependent oligomerization of nucleosomal arrays. *J. Biol. Chem.* **280**, 33701–33706, doi:10.1074/jbc.M507048200 (2005).

53 Li, S., Aristizabal, M. J., Grigoryev, S. A. & Panchenko, A. R. Molecular Dynamics-Guided All-Atom Reconstruction of Cryo-ET Maps Reveals Mechanisms of Histone Tail-Mediated Chromatin Compaction. *bioRxiv*, 2025.2011.2005.686627, doi:10.1101/2025.11.05.686627 (2025).

54 Farcaş, A.-A. & Bende, A. in *Adv. Quantum Chem.* Vol. 81 269–290 (Elsevier, 2020).

55 Ong, M. S., Vasudevan, D. & Davey, C. A. Divalent metal- and high mobility group N protein-dependent nucleosome stability and conformation. *Nucleic Acids Res.* **2010**, 143890, doi:10.4061/2010/143890 (2010).

56 Liang, Q. & Dedon, P. C. Cu(II)/H2O2-induced DNA damage is enhanced by packaging of DNA as a nucleosome. *Chem. Res. Toxicol.* **14**, 416–422, doi:10.1021/tx0002278 (2001).

57 Gibney, A. *et al.* A Click Chemistry-Based Artificial Metallo-Nuclease. *Angew. Chem. Int. Ed. Engl.* **62**, e202305759, doi:10.1002/anie.202305759 (2023).

58 Gelagutashvili, E. S., Sigua, K. I. & Sapojnikova, N. A. Binding and the nature of Cu(II) ion interaction with nucleosomes. *J. Inorg. Biochem.* **70**, 207–210, doi:10.1016/s0162-0134(98)10016-8 (1998).

59 Govindaraju, M. *et al.* Copper interactions with DNA of chromatin and its role in neurodegenerative disorders. *J Pharm Anal* **3**, 354–359, doi:10.1016/j.jpha.2013.03.003 (2013).

60 Li, S., Olson, W. K. & Lu, X. J. Web 3DNA 2.0 for the analysis, visualization, and modeling of 3D nucleic acid structures. *Nucleic Acids Res.* **47**, W26–W34, doi:10.1093/nar/gkz394 (2019).

61 Fuchs, H. A. *et al.* G34R cancer mutation alters the conformational ensemble and dynamics of the histone H3.3 tails. *bioRxiv*, 2025.2005.2002.651932, doi:10.1101/2025.05.02.651932 (2025).

62 Maier, J. A. *et al.* ff14SB: Improving the Accuracy of Protein Side Chain and Backbone Parameters from ff99SB. *J. Chem. Theory Comput.* **11**, 3696–3713, doi:10.1021/acs.jctc.5b00255 (2015).

63 Galindo-Murillo, R. *et al.* Assessing the Current State of Amber Force Field Modifications for DNA. *J. Chem. Theory Comput.* **12**, 4114–4127, doi:10.1021/acs.jctc.6b00186 (2016).

64 Li, S., Wei, T. & Panchenko, A. R. Histone variant H2A.Z modulates nucleosome dynamics to promote DNA

accessibility. *Nat. Commun.* **14**, 769, doi:10.1038/s41467-023-36465-5 (2023).

65 Li, S., Peng, Y., Landsman, D. & Panchenko, A. R. DNA methylation cues in nucleosome geometry, stability and unwrapping. *Nucleic Acids Res.* **50**, 1864–1874, doi:10.1093/nar/gkac097 (2022).

66 Kohestani, H. & Wereszczynski, J. Effects of H2A.B incorporation on nucleosome structures and dynamics. *Biophys. J.* **120**, 1498–1509, doi:10.1016/j.bpj.2021.01.036 (2021).

67 Rabdano, S. O. *et al.* Histone H4 Tails in Nucleosomes: a Fuzzy Interaction with DNA. *Angew. Chem. Int. Ed. Engl.* **60**, 6480–6487, doi:10.1002/anie.202012046 (2021).

68 Horn, H. W. *et al.* Development of an improved four-site water model for biomolecular simulations: TIP4P-Ew. *J. Chem. Phys.* **120**, 9665–9678, doi:10.1063/1.1683075 (2004).

69 Li, P., Song, L. F. & Merz, K. M., Jr. Systematic Parameterization of Monovalent Ions Employing the Nonbonded Model. *J. Chem. Theory Comput.* **11**, 1645–1657, doi:10.1021/ct500918t (2015).

70 Li, P., Roberts, B. P., Chakravorty, D. K. & Merz, K. M., Jr. Rational Design of Particle Mesh Ewald Compatible Lennard-Jones Parameters for +2 Metal Cations in Explicit Solvent. *J. Chem. Theory Comput.* **9**, 2733–2748, doi:10.1021/ct400146w (2013).

71 Li, P. & Merz Jr, K. M. Taking into account the ion-induced dipole interaction in the nonbonded model of ions. *J. Chem. Theory Comput.* **10**, 289–297 (2014).

72 Li, P., Song, L. F. & Merz, K. M., Jr. Parameterization of highly charged metal ions using the 12-6-4 LJ-type nonbonded model in explicit water. *J. Phys. Chem. B* **119**, 883–895, doi:10.1021/jp505875v (2015).

73 Kantakevičius, P., Mathiah, C., Johannissen, L. O. & Hay, S. Chelator-Based Parameterization of the 12-6-4 Lennard-Jones Molecular Mechanics Potential for More Realistic Metal Ion-Protein Interactions. *J. Chem. Theory Comput.* **18**, 2367–2374, doi:10.1021/acs.jctc.1c00898 (2022).

74 Panteva, M. T., Giambasu, G. M. & York, D. M. Force field for Mg2+, Mn2+, Zn2+, and Cd2+ ions that have balanced interactions with nucleic acids. *J. Phys. Chem. B* **119**, 15460–15470 (2015).

75 Schwartz, E. A. *et al.* RNA targeting and cleavage by the type III-Dv CRISPR effector complex. *Nat. Commun.* **15**, 3324, doi:10.1038/s41467-024-47506-y (2024).

76 Zhang, J., Fakharzadeh, A., Pan, F., Roland, C. & Sagui, C. Atypical structures of GAA/TTC trinucleotide repeats underlying Friedreich's ataxia: DNA triplexes and RNA/DNA hybrids. *Nucleic Acids Res.* **48**, 9899–9917, doi:10.1093/nar/gkaa665 (2020).

77 Song, L. F., Sengupta, A. & Merz, K. M., Jr. Thermodynamics of Transition Metal Ion Binding to Proteins. *J. Am. Chem. Soc.* **142**, 6365–6374, doi:10.1021/jacs.0c01329 (2020).

78 Cruz-León, S. & Schwierz, N. RNA Captures More Cations than DNA: Insights from Molecular Dynamics Simulations. *J. Phys. Chem. B* **126**, 8646–8654, doi:10.1021/acs.jpcb.2c04488 (2022).

79 Salomon-Ferrer, R., Case, D. A. & Walker, R. C. An overview of the Amber biomolecular simulation package. *WIREs Comput. Mol. Sci.* **3**, 198–210, doi:https://doi.org/10.1002/wcms.1121 (2013).

80 Turq, P., Lantelme, F. & Friedman, H. L. Brownian dynamics: Its application to ionic solutions. *J. Chem. Phys.* **66**, 3039–3044 (1977).

81 Berendsen, H. J. C., Postma, J. P. M., van Gunsteren, W. F., DiNola, A. & Haak, J. R. Molecular dynamics with coupling to an external bath. *J. Chem. Phys.* **81**, 3684–3690, doi:10.1063/1.448118 (1984).

82 Essmann, U. *et al.* A smooth particle mesh Ewald method. *J. Chem. Phys.* **103**, 8577–8593, doi:10.1063/1.470117 (1995).

83 Ryckaert, J.-P., Ciccotti, G. & Berendsen, H. J. C. Numerical integration of the cartesian equations of motion

of a system with constraints: molecular dynamics of n-alkanes. *J. Comput. Phys.* **23**, 327–341, doi:https://doi.org/10.1016/0021-9991(77)90098-5 (1977).

84 Humphrey, W., Dalke, A. & Schulten, K. VMD: Visual molecular dynamics. *J. Mol. Graph.* **14**, 33–38, doi:https://doi.org/10.1016/0263-7855(96)00018-5 (1996).

85 Grant, B. J., Rodrigues, A. P., ElSawy, K. M., McCammon, J. A. & Caves, L. S. Bio3d: an R package for the comparative analysis of protein structures. *Bioinformatics* **22**, 2695–2696, doi:10.1093/bioinformatics/btl461 (2006).

86 Pitman, M., Dalal, Y. & Papoian, G. A. Minimal Cylinder Analysis Reveals the Mechanical Properties of Oncogenic Nucleosomes. *Biophys. J.* **118**, 2309–2318, doi:10.1016/j.bpj.2020.01.042 (2020).

87 Ahadi, A., Johansson, D. & Evilevitch, A. Modeling and simulation of the mechanical response from nanoindentation test of DNA-filled viral capsids. *J. Biol. Phys.* **39**, 183–199, doi:10.1007/s10867-013-9297-9 (2013).

88 Li, L. *et al.* DelPhiForce web server: electrostatic forces and energy calculations and visualization. *Bioinformatics* **33**, 3661–3663, doi:10.1093/bioinformatics/btx495 (2017).

89 Hu, G. Y., Peng. Selective Binding of Divalent Cations Reshapes Nucleosome Mechanics and Unlocks Histone Tail Dynamics. *Zenodo* doi:10.5281/zenodo.18232757.

Acknowledgement

This work was supported by the National Natural Science Foundation of China (No. 12205112) , the Natural Science Foundation of Wuhan (No.2024040801020302) and the self-determined research funds of CCNU from the colleges'basic research and operation of MOE (CCNU25JC005).

Author Contributions

Y.H.P. conceived and designed the research, performed simulations, analyzed the data, wrote the manuscript, and acquired funding. G.H.H. performed simulations, analyzed the data, and wrote the manuscript. W.X., G.G.L., and H.F.Z. contributed to data analysis and interpretation.

Competing interests

The authors declare no competing interests.

Figure 1. Distinct spatial distribution patterns of divalent ions around the nucleosome.
(a) Schematic of the simulated nucleosome systems under different ionic conditions. Left: 26 mM Ca^{2+} with 150 mM NaCl; Right: 17 mM Mg^{2+} with 150 mM NaCl. (b) Radial distribution functions (RDFs) of Ca^{2+} and Mg^{2+} around the nucleosome computed from simulations using the 12–6 and m12–6–4 models. RDFs of Na^{+} are shown as blue and orange dashed lines, representing Na^{+} distributions in two independent simulation systems (12–6 vs. m12–6–4 models). Values represent averages over three independent simulations (n = 3).

Figure 2. Binding modes of divalent cations in the nucleosome.
(a) Schematic representation of distinct binding modes of divalent ions within the nucleosome. (b) Occupancy of Ca^{2+} and Mg^{2+} across nucleosomal DNA, histones, and DNA–histone interface regions, shown as percentages and absolute numbers. (c) Average numbers of bound Ca^{2+} and Mg^{2+} ions in each binding mode. Values represent mean ± SEM (Standard Error of the Mean) from three independent simulations (n = 3).

Figure 3. Binding of divalent ions alters nucleosomal DNA gyre spacing.
(a) Schematic of the nucleosome highlighting the superhelical locations (SHLs) used for gyre-gaping distance measurements (pink). The right panel illustrates gaping distances measured between SHL +4 and SHL –4. (b) Comparison of DNA gyre gaping distances at selected SHLs in tailless nucleosomes, in the absence and presence of Mg^{2+}. For each run, gaping distances were averaged over simulation time, and the reported values represent the mean ± SEM across three independent simulations (n = 3). (c) Projected electrostatic forces between upper and lower DNA gyres at different SHLs, calculated along the vector connecting the gyre centroids from frames containing a single bound Mg^{2+}. Forces were computed both with the Mg^{2+} present and after its removal. Box plots show distributions pooled from three independent simulations. Each point corresponds to one simulation frame in which a single Mg^{2+} is bound at the

specified SHL (n(SHL –2) = 130, n(SHL –4) = 91, and n(SHL –6) = 115). Statistical significance was assessed using Welch's two-sample t-test (*** corresponding to $p < 0.001$). Exact p-values and effect sizes (Cohen's d) were: SHL −2, $p = 7.79 \times 10^{-16}$, $d = -1.07$; SHL −4, $p = 1.76 \times 10^{-9}$, $d = -0.94$; SHL −6, $p = 9.38 \times 10^{-15}$, $d = -1.09$. Box plots: center line, median; box limits, upper and lower quartiles; whiskers extend to 1.5× interquartile range.

Figure 4. Divalent ions modulate nucleosome plasticity and compaction.
(a) Schematic of the nucleosome approximated as a cylinder, with height and radius measured for structural analysis. (b) Young's modulus of tailless nucleosomes in the absence and presence of Mg^{2+}. Values represent mean ± SEM across three independent simulations (n = 3). (c) Box plots of nucleosome height for tailless nucleosomes, pooled from three independent simulations. Each data point represents the nucleosome height calculated from a 400-ns trajectory segment (n(NaCl) = 72, n(Mg^{2+}) = 68). Statistical significance was assessed using Welch's two-sample t-test (*** corresponding to $p < 0.001$). Exact p-value and effect size (Cohen's d) were: $p = 1.53 \times 10^{-36}$, $d = -2.92$. (d) Correlation between nucleosome height and Young's modulus, indicating that vertical compaction contributes to increased mechanical stiffness. (e) Dynamic cross-correlation matrices (DCCMs) of DNA phosphate atoms in tailless nucleosomes without and with Mg^{2+}. Data from all three independent simulations were combined for analysis. Box plots: center line, median; box limits, upper and lower quartiles; whiskers extend to 1.5× interquartile range.

Figure 5. Divalent ions weaken histone tail–DNA interactions and enhance nucleosome dynamics.
(a) Average number of contacts between H3 tail and DNA. (b) Binding free energy between the H3 tail and DNA. (c) Average number of DNA contacts per residue for H3 tail. Panels (a–c) show mean ± SEM from three independent simulations , averaged over the two H3 tails per nucleosome (n = 6). (d) Representative H3 tail conformations under different ionic conditions, sampled every 10 ns. (e) H3 tail–DNA residence time. Each point represents an individual binding event observed across three independent simulations for both H3 tail copies (n(NaCl) = 7, n(Ca^{2+}) = 11, n(Mg^{2+}) = 12). (f) Total number of full H3 tail-DNA binding events. Panels (d–f) represent aggregated data from three independent simulations, accounting for both H3 tails in each nucleosome. Box plots: center line, median; box limits, upper and lower quartiles; whiskers extend to 1.5× interquartile range.

Figure 6. Proposed model of divalent cation–mediated regulation of chromatin.
Divalent cations alter nucleosomal DNA gyre spacing and modulate histone tail–DNA interactions, thereby tuning nucleosome plasticity and accessibility. These effects may influence higher-order chromatin organization and the recruitment of chromatin remodelers and epigenetic regulators.

Editorial summary:

Nucleosome plasticity is critical for many chromatin-related processes. The authors demonstrate how biologically relevant divalent ions reshape nucleosome structure and mechanical stiffness.

Peer review information:

Communications Biology thanks Mateusz Kogut, Damien Thompson and Stephanie Portillo-Ledesma for

their contribution to the peer review of this work. Primary Handling Editors: Michal Kolar and Laura Rodríguez Pérez.

a

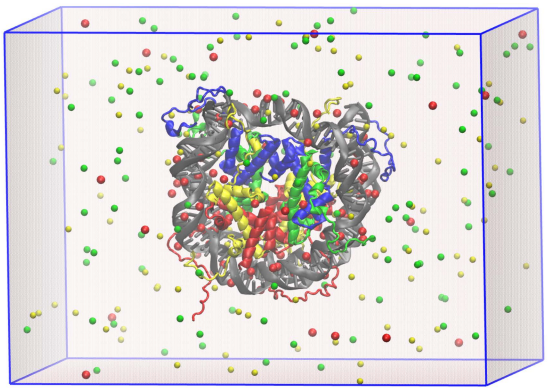

Ca^{2+} Na^{+} Cl^{-}

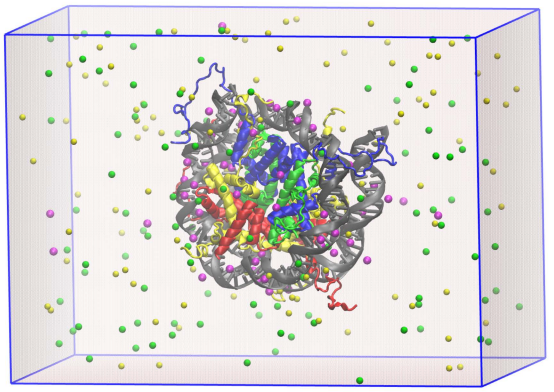

Mg^{2+} Na^{+} Cl^{-}

b

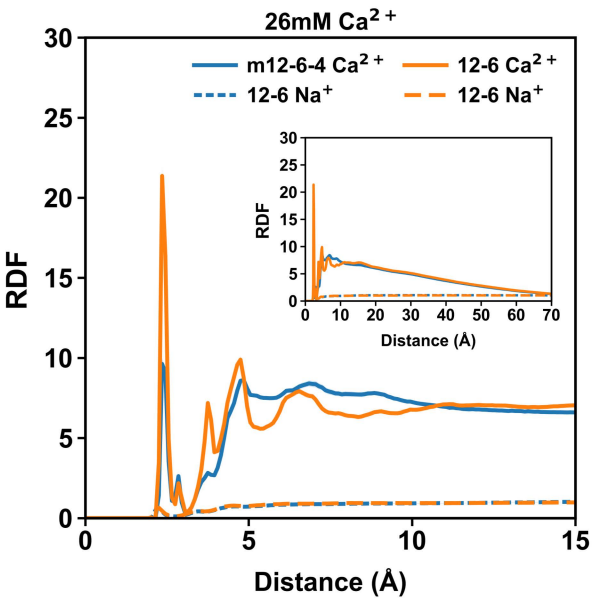

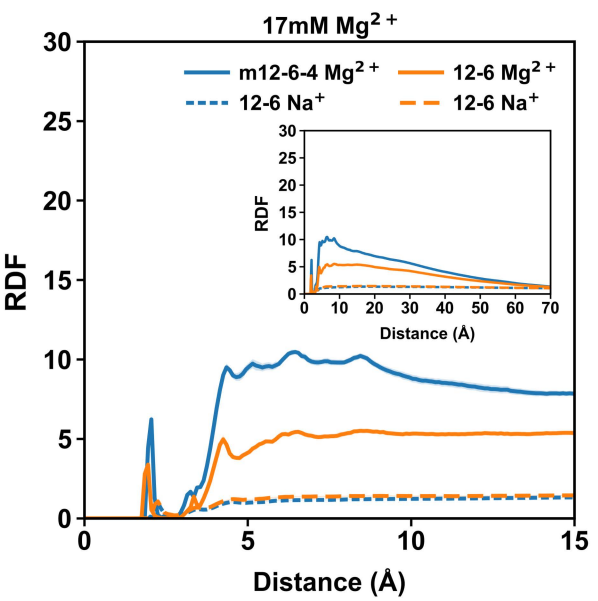

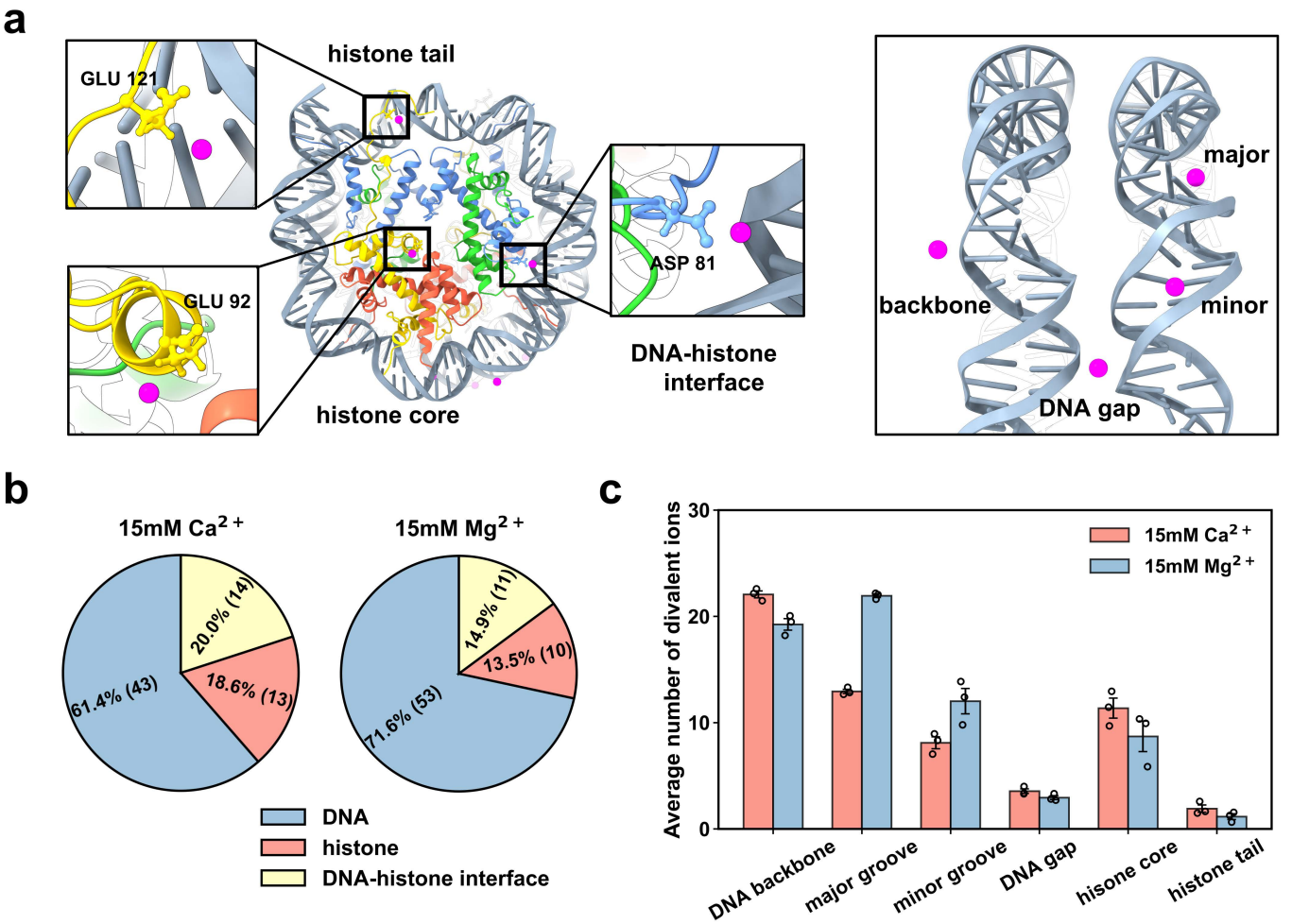
a
GLU 121
histone tail
GLU 92
ASP 81
DNA-histone interface
histone core
major
backbone
minor
DNA gap
b
15mM Ca2 +
15mM Mg2 +
20.0% (14)
18.6% (13)
61.4% (43)
14.9% (11)
13.5% (10)
71.6% (53)
DNA
histone
DNA-histone interface
c
Average number of divalent ions
30
20
10
0
15mM Ca2 +
15mM Mg2 +
DNA backbone
major groove
minor groove
DNA gap
hisone core
histone tail

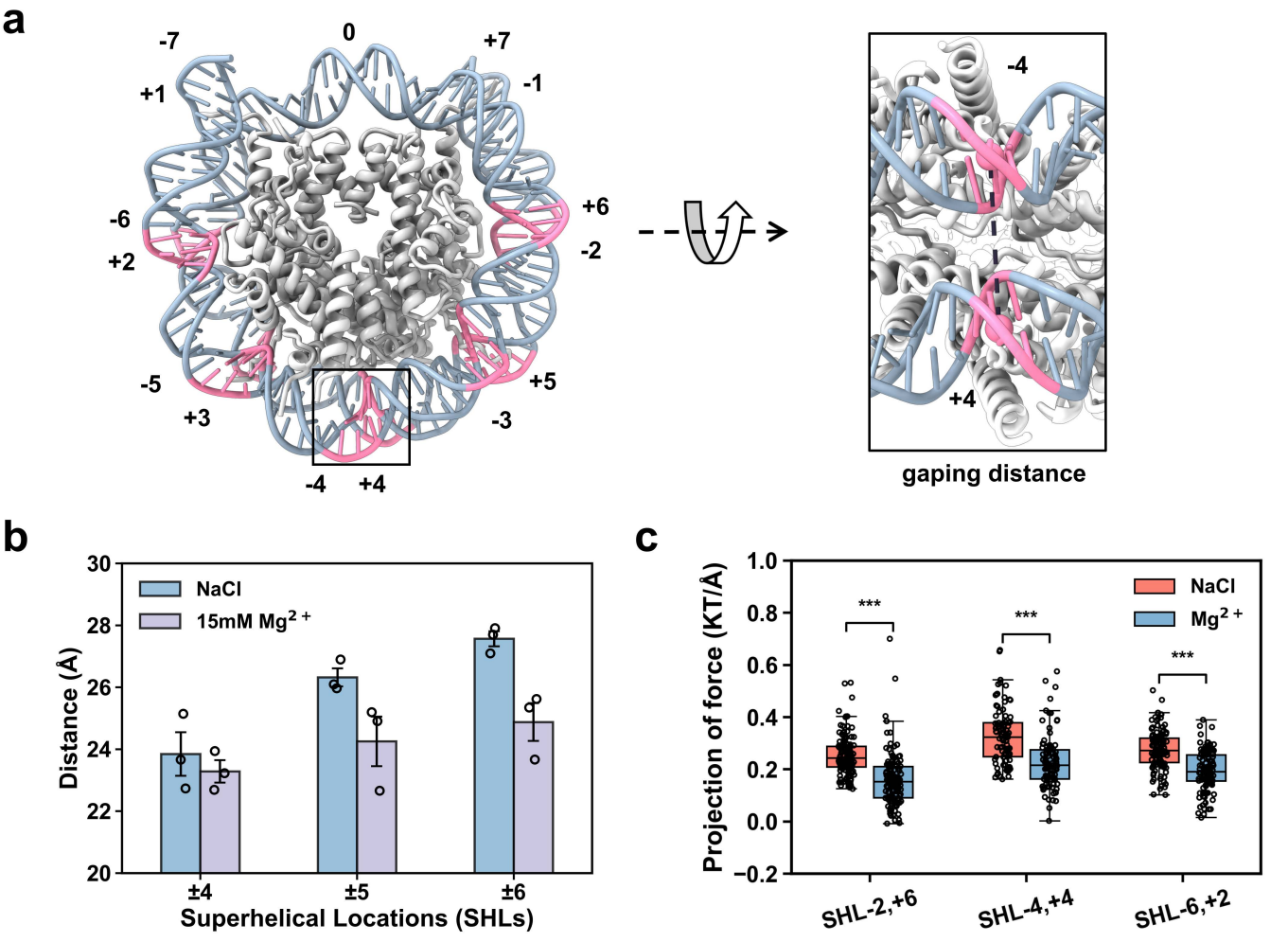
a
-7
0
+7
+1
-1
-6
+6
+2
-2
-5
+5
+3
-3
-4
+4
-4
+4
gaping distance
b
NaCl
15mM Mg2+
Distance (Å)
30
28
26
24
22
20
±4
±5
±6
Superhelical Locations (SHLs)
c
NaCl
Mg2+
Projection of force (KT/Å)
1.0
0.8
0.6
0.4
0.2
0.0
−0.2
***
***
***
SHL-2,+6
SHL-4,+4
SHL-6,+2

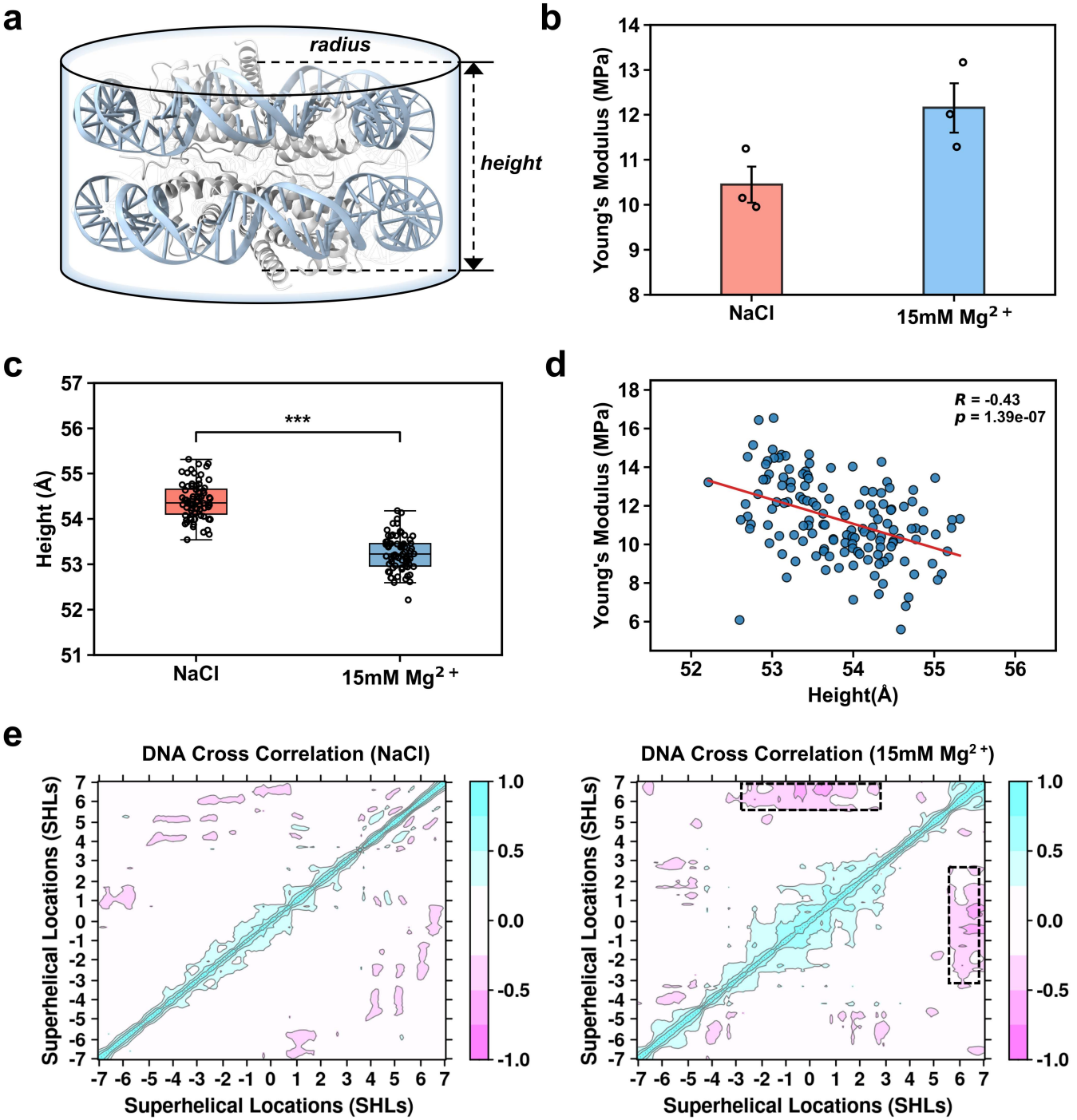
a
radius
height
b
Young's Modulus (MPa)
NaCl
15mM Mg2 +
c
Height (Å)
***
NaCl
15mM Mg2 +
d
R = -0.43
p = 1.39e-07
Young's Modulus (MPa)
Height(Å)
e
DNA Cross Correlation (NaCl)
DNA Cross Correlation (15mM Mg2 +)
Superhelical Locations (SHLs)
Superhelical Locations (SHLs)

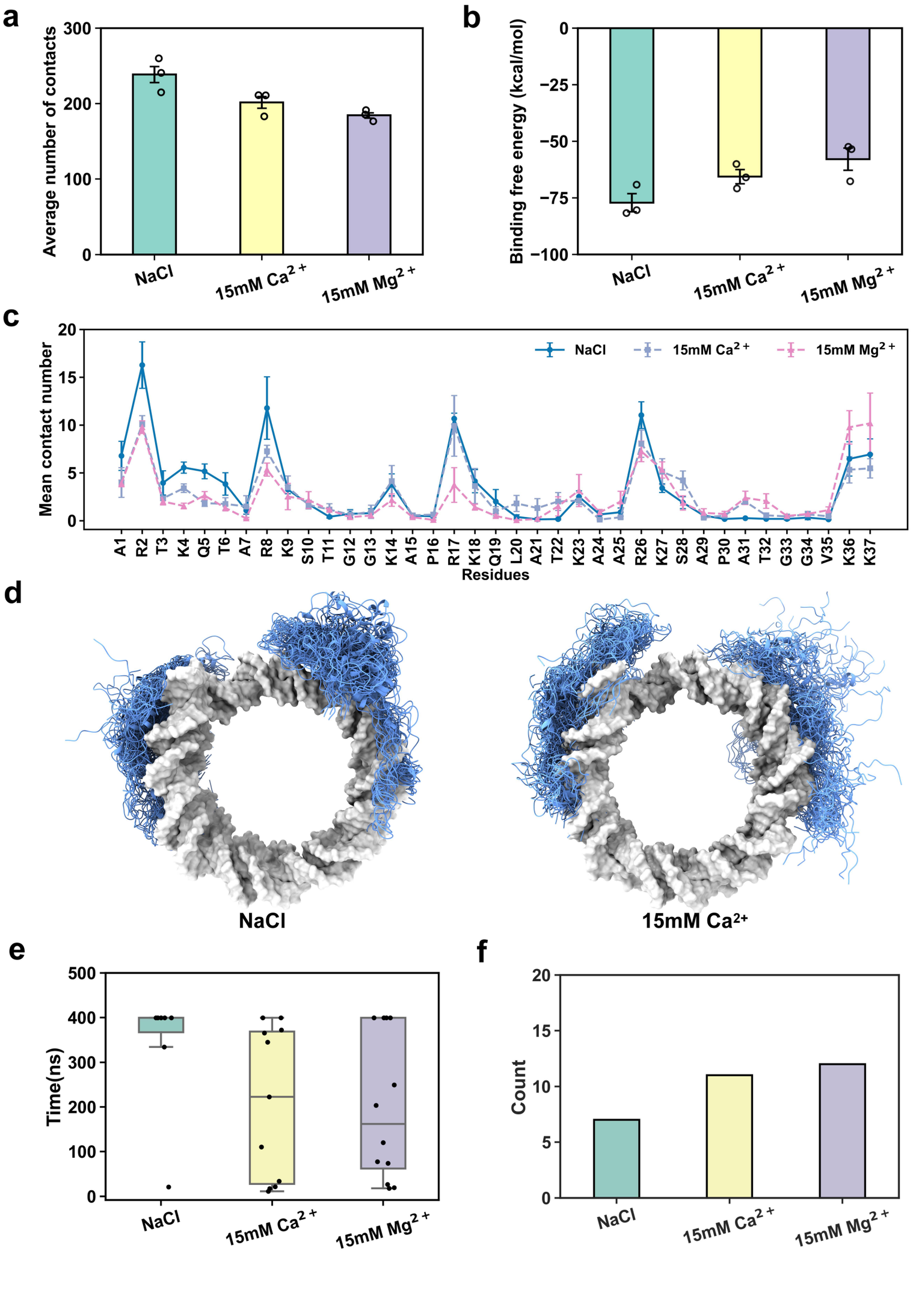
a
Average number of contacts
300
200
100
0
NaCl
15mM Ca2+
15mM Mg2+
b
Binding free energy (kcal/mol)
0
−25
−50
−75
−100
NaCl
15mM Ca2+
15mM Mg2+
c
Mean contact number
20
15
10
5
0
NaCl
15mM Ca2+
15mM Mg2+
A1 R2 T3 K4 Q5 T6 A7 R8 K9 S10 T11 G12 G13 K14 A15 P16 R17 K18 Q19 L20 A21 T22 K23 A24 A25 R26 K27 S28 A29 P30 A31 T32 G33 G34 V35 K36 K37
Residues
d
NaCl
15mM Ca2+
e
Time(ns)
500
400
300
200
100
0
NaCl
15mM Ca2+
15mM Mg2+
f
Count
20
15
10
5
0
NaCl
15mM Ca2+
15mM Mg2+

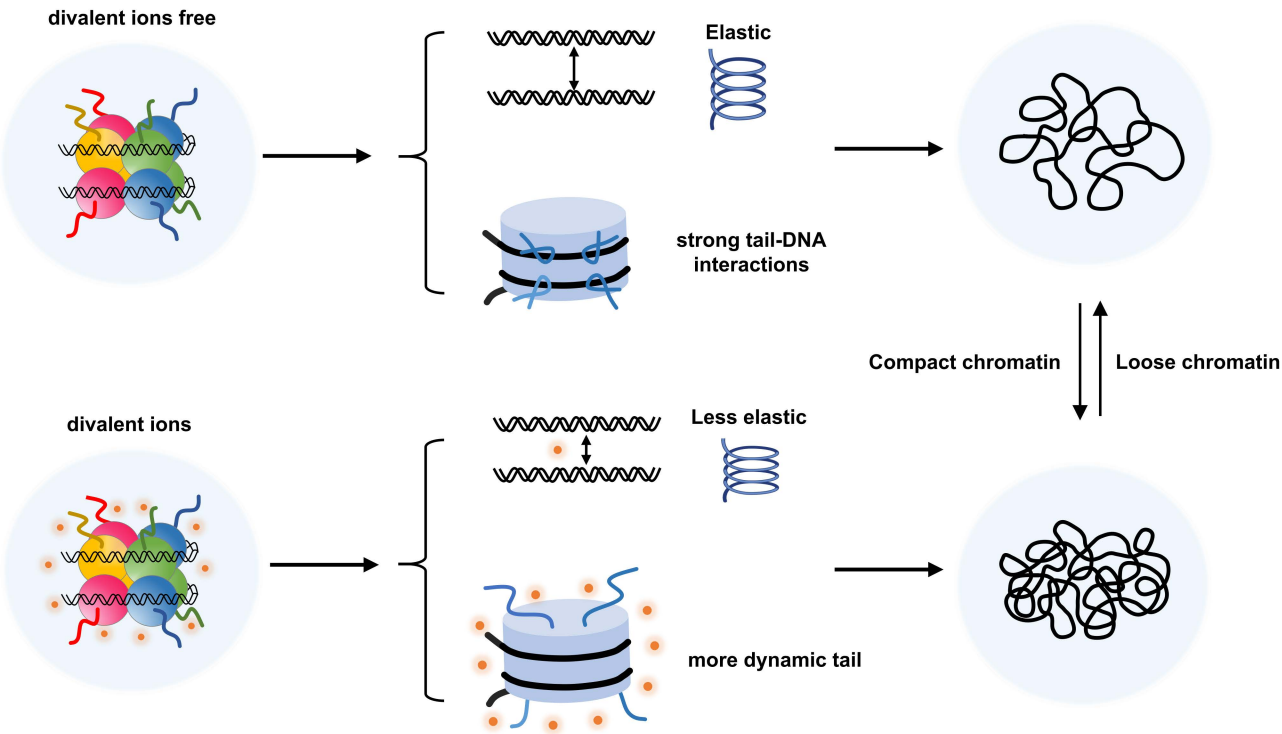
divalent ions free
Elastic
strong tail-DNA interactions
Compact chromatin
Loose chromatin
divalent ions
Less elastic
more dynamic tail

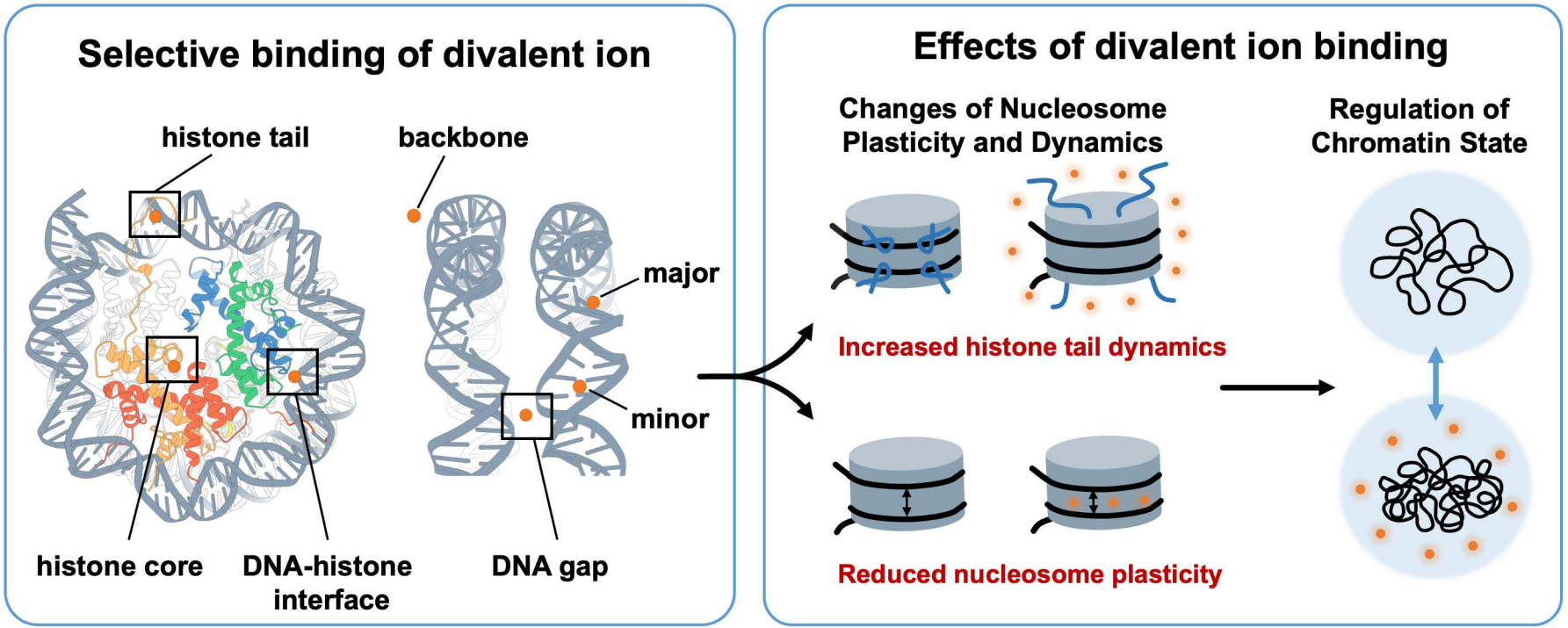
Selective binding of divalent ion
histone tail
backbone
major
minor
histone core
DNA-histone interface
DNA gap
Effects of divalent ion binding
Changes of Nucleosome Plasticity and Dynamics
Regulation of Chromatin State
Increased histone tail dynamics
Reduced nucleosome plasticity